

# Journal of Geophysical Research: Space Physics

## RESEARCH ARTICLE

10.1002/2015JA021387

**Key Points:**

- Inner radiation belt electrons were measured by SAMPEX/PET during 1992–2009
- Following the 2003 Halloween storm they were not observed above 1 MeV but may have been present
- Less stably trapped electrons were seen at other times with soft energy spectra up to 1.6 MeV

**Correspondence to:**R. S. Selesnick,  
richard.selesnick@us.af.mil**Citation:**Selesnick, R. S. (2015), Measurement of inner radiation belt electrons with kinetic energy above 1 MeV, *J. Geophys. Res. Space Physics*, 120, 8339–8349, doi:10.1002/2015JA021387.

Received 28 APR 2015

Accepted 4 SEP 2015

Accepted article online 10 SEP 2015

Published online 3 OCT 2015

## Measurement of inner radiation belt electrons with kinetic energy above 1 MeV

**R. S. Selesnick<sup>1</sup>**<sup>1</sup>Space Vehicles Directorate, Air Force Research Laboratory, Kirtland AFB, New Mexico, USA

**Abstract** Data from the Proton-Electron Telescope on the Solar, Anomalous, and Magnetospheric Particle Explorer (SAMPEX) satellite, taken during 1992–2009, are analyzed for evidence of inner radiation belt electrons with kinetic energy  $E > 1$  MeV. It is found that most of the data from a detector combination with a nominal energy threshold of 1 MeV were, in fact, caused by a chance coincidence response to lower energy electrons or high-energy protons. In particular, there was no detection of inner belt or slot region electrons above 1 MeV following the 2003 Halloween storm injection, though they may have been present. However, by restricting data to a less-stable, low-altitude trapping region, a persistent presence of inner belt electrons in the energy range 1 to 1.6 MeV is demonstrated. Their soft, exponential energy spectra are consistent with extrapolation of lower energy measurements.

### 1. Introduction

Recent measurements from Van Allen Probes have shown that inner radiation belt electron intensity for kinetic energy  $E > 1$  MeV has, since 2012, been below detectable levels [Li *et al.*, 2015; Fennell *et al.*, 2015]. The result is in contradiction to empirical radiation belt models that predict levels higher than the upper limits available from Van Allen Probes data and are based on combined measurements from extended time periods [Vette, 1991; Ginet *et al.*, 2013]. Data analysis is complicated by the presence of intense high-energy radiation belt protons, regardless of measurement technique. For this reason, the question of whether earlier inner belt electron measurements were in error, or whether the trapped electron intensity has decreased substantially in recent years, remains unanswered.

An extended set of radiation belt electron data was collected by the Proton-Electron Telescope (PET) on the low-altitude Solar, Anomalous, and Magnetospheric Particle Explorer (SAMPEX) satellite [Baker *et al.*, 1993; Cook *et al.*, 1993]. It provided nearly continuous coverage from its launch in mid-1992 until instrument failure in late-2009. Results from PET provided convincing evidence of remnant trapped electrons from the March 1991 injection, with  $E > 15$  MeV, and their decay over a period of several years [Looper *et al.*, 1994, 2005]. However, this was an isolated event and does not address the question of whether there was a steady or even intermittent presence of inner belt electrons near or above 1 MeV, which is the subject of this work.

Several studies of an apparent injection of ~2 to 6 MeV electrons into the slot region and inner belt during the 2003 Halloween magnetic storm were based on PET data [Baker *et al.*, 2004, 2007; Looper *et al.*, 2005; Horne *et al.*, 2005; Loto'aniu *et al.*, 2006; Shprits *et al.*, 2006; Zheng *et al.*, 2006]. They made reasonable assumptions about the data validity but, given recent developments, it is of interest to now review these measurements with additional scrutiny. This requires an analysis of potential errors that can occur in the data interpretation. It begins in section 2 with a description of the trapping regions accessible to SAMPEX; section 3 describes the nominal PET response to energetic electrons; sections 4 and 5, respectively, present analyses of the PET rate and event data types, with particular attention to the problem of chance coincidences; section 6 describes measurement of trapped electron energy spectra by PET; finally, results and conclusions are summarized in section 7.

### 2. Trapping Regions

A low-altitude satellite encounters stably trapped radiation belt particles in the South Atlantic Anomaly (SAA), a region of low magnetic field where trapped particles attain their lowest altitude. It is important to separate the stable trapping region from other regions so that average trapped particle intensities can be accurately

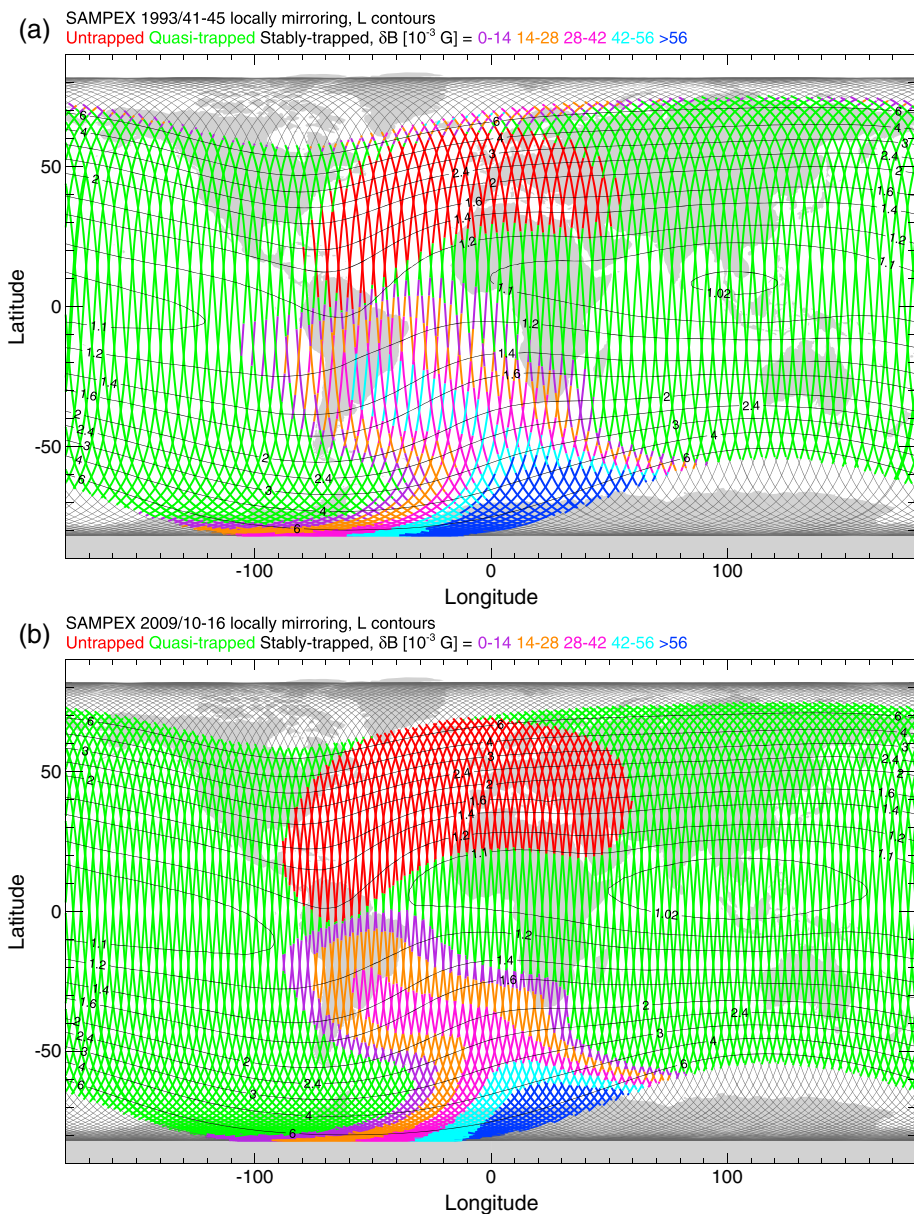


**Figure 1.** Maps showing SAMPEX satellite ground tracks during (a) 1993 days-of-year 41 to 45 and (b) 2009 days-of-year 10 to 16. For  $L < 8$ , tracks are color coded to show regions where radiation belt particles are stably trapped (multicolored), quasi-trapped (green), or untrapped (red). The stable trapping regions are subdivided by ranges of  $\delta B$  (defined in the text). For example, the least stable trapping-region (purple) has  $0 < \delta B < 0.014 \text{ G}$  and the most stable (blue) has  $\delta B > 0.056 \text{ G}$ . Labeled contours of constant  $L$  shell are also shown.

computed. For this work, the stable trapping region is further subdivided, as described below, in order to separate valid and invalid electron measurements.

Following convention, a particle is considered to be stably trapped if it follows a drift shell with a minimum altitude above 100 km. If a particle will reach below 100 km during its drift motion but must pass more than a single mirror point from its current location to do so, then it is said to be quasi-trapped. If it will reach below 100 km before mirroring, then it is untrapped. Each drift shell is labeled by  $L$  and the mirror magnetic field  $B_m$  [Roederer, 1970]. For particles that mirror at a satellite (local mirroring),  $B_m$  is the local field magnitude  $B$ . Other particles reach the satellite mirror at lower altitude and higher  $B_m$ .

Trapping regions for locally mirroring particles are defined by comparing  $B$  to  $B_{100}$ , the minimum north or south field magnitude of the local field line 100-km altitude foot points, and to  $B'_{100}$ , the minimum north or

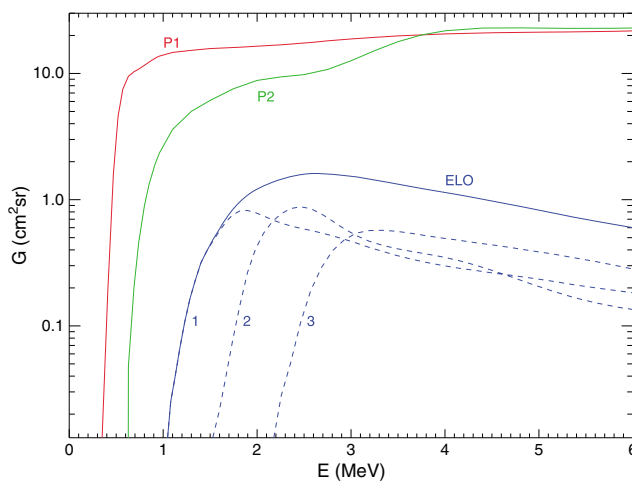


**Figure 2.** Geometry factors  $G$  as a function of electron kinetic energy  $E$  describing the nominal response of SAMPEX/PET data types P1 (red), P2 (green), and ELO (blue). The ELO response is subdivided into channels 1, 2, and 3 (dashed).

south 100 km altitude field magnitudes at any location on the entire drift shell defined by  $B$  and  $L$ . Stably trapped particles have  $B'_{100} > B$ , quasi-trapped have  $B_{100} > B > B'_{100}$ , and untrapped have  $B > B_{100}$ . Examples for the SAMPEX satellite are shown in Figure 1. Satellite ground tracks are shown over a world map and color coded to distinguish (for  $L < 8$ ) regions of locally mirroring particles that are untrapped, quasi-trapped, or stably trapped. Separate maps are shown for a period in 1993 (Figure 1a), near the start of the PET data set, and in 2009 (Figure 1b), near the end of the data set. Regions of stable trapping are subdivided according to the value of  $\delta B = B'_{100} - B$ . Larger values of  $\delta B$  correspond to particles mirroring at higher altitude which are therefore more stably trapped.

The SAMPEX orbit was not circular and precessed with a  $\sim 3$  month period. It decayed and circularized during the satellite lifetime. There were times when ascending and descending orbital tracks over the SAA occurred at significantly different altitudes and had dissimilar trapping regions, as in Figure 1a (overall altitude range 518 to 686 km). At other times they were closer in altitude and had similar trapping regions, as in Figure 1b (overall altitude range 428 to 512 km). Contours of constant  $L$ , also shown in the figure, were computed for the higher-altitude ascending tracks. All field computations were made with the IGRF model [Finlay et al., 2010] and  $L$  values were defined with the McIlwain formula and the geomagnetic dipole moment of date [Roederer, 1970]. The inner radiation belt is roughly defined by  $L < 2$ , the slot region by  $2 < L < 3$ , and the outer belt by  $L > 3$ .

### 3. Response Functions

The PET sensor consists of a series of eight aligned Li-drifted silicon detectors. Only data from the first two detectors, called P1 and P2, are considered in this work. They are each 0.2 cm thick, have  $8 \text{ cm}^2$  active area, are separated by  $\sim 5.2$  cm, are spherically curved to minimize path length variations between particles with different incidence angles, and together form a  $58^\circ$  (full angle) field of view. They operate individually and in coincidence. Individually, they trigger the P1 and P2 rate counters. When they are triggered in coincidence, within a resolving time  $\tau$ , with a low-energy deposit in P1 (defined below), and the third detector P3 is not triggered, a count is registered in a data type called ELO, meaning low-energy electrons. (There are also proton data types, such as PLO, and higher-energy electron data types, such as EHI requiring coincidence of the first three detectors.) See Cook et al. [1993] for details on all aspects of the PET instrument.

Energy response functions, or geometry factors  $G$ , describe the efficiency as a function of incident energy for measuring an isotropic distribution of electrons in each data type. These are shown in Figure 2 for the P1 and P2 detectors operating individually and for the ELO combination. For computing energy spectra (see section 6), the ELO response is subdivided into three channels (dashed lines in the figure) that measure electrons with successively higher-energy thresholds. They were defined specifically for this work by requiring that the sum of measured energy loss within each detector be above similar thresholds. All electrons triggering ELO fall into one of these channels. All of the response functions were determined from calibration data taken at electron beam facilities prior to the launch of SAMPEX. Angular response functions for anisotropic distributions are also available [Selesnick et al., 2003] but are not used in this work.

The ELO data type has often been described as measuring 2 to 6 MeV electrons [e.g., Baker et al., 2007]. The response function shows that the true threshold for ELO is approximately 1.04 MeV. This difference is

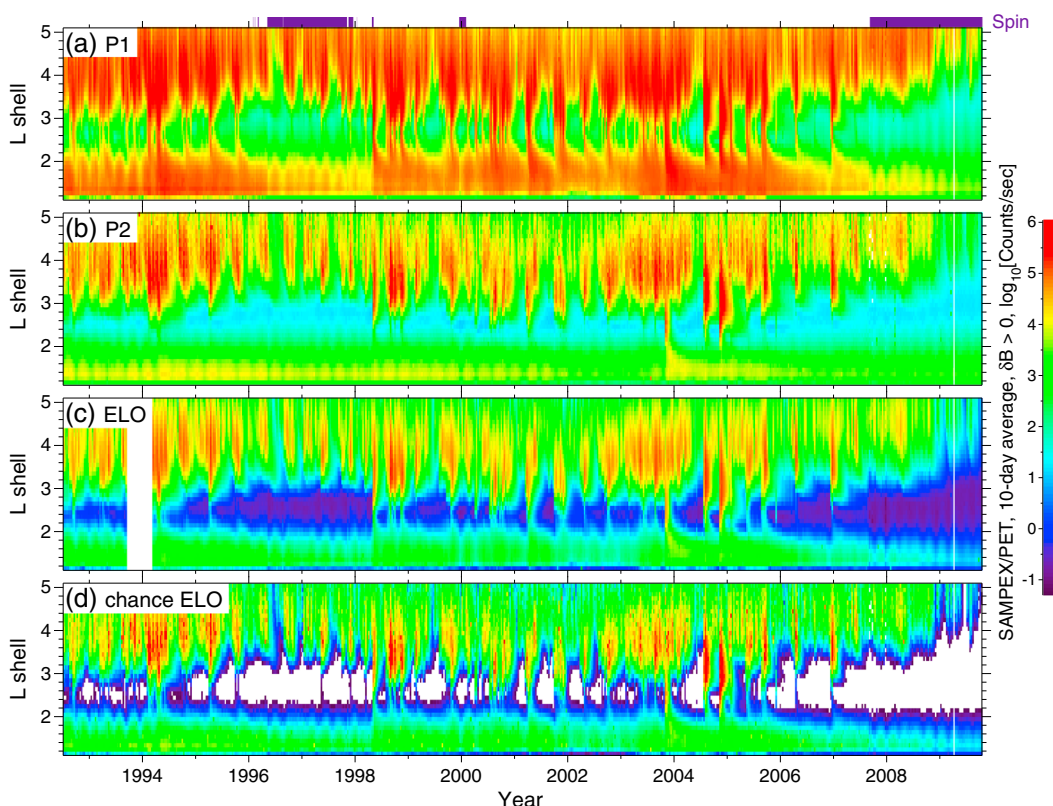


**Figure 3.** Measured average rates from the (a) P1, (b) P2, and (c) ELO data types, and (d) the computed chance coincidence ELO rate, as a function of  $L$  shell and time (labeled at the start of even-numbered years). Data from the entire stable trapping region ( $\delta B > 0$ ) are included. Intervals when SAMPEX was spinning at 1 RPM are indicated by the bar at the top.

significant for the soft electron spectra observed in the inner radiation belt [Fennell et al., 2015]. The three defined ELO channels (dashed lines) have thresholds of approximately 1.04, 1.53, and 2.17 MeV. The P1 and P2 response functions have thresholds of approximately 0.35 and 0.63 MeV, respectively.

#### 4. Rate Data

Counting rate data are available from P1, P2, and ELO with 6 s resolution. Each data point is an accumulation of counts during a 6 s interval. It is converted to a rate, or particle flux in counts/s, after dividing by the instrument live time (a variable interval  $\leq 6$  s during which particles can be counted and which decreases at higher flux levels). Live time is determined by the ratio of observed to expected counts from a steady pulser. Data coverage for P1 and ELO is continuous, except for occasional data gaps; for P2 it is one data point in every eight 6 s intervals.

Rate data from P1, P2, and ELO are shown in Figures 3a, 3b, and 3c, respectively. They are taken only from the stable trapping region as illustrated in Figure 1, that is,  $\delta B > 0$  for each included data point. The data are averaged over 10 day and  $0.1L$  intervals and shown as color-coded values versus  $L$  and time. All available data, from 1992 through 2009, are included.

Several factors should be considered for accurate interpretation of the data in Figure 3:

1. Usually, PET was pointed nearly perpendicular to magnetic field during radiation belt passes. However, there were times when SAMPEX was spinning at 1 RPM, mainly in 1996–1997 and after 2007 as indicated in the figure. Then PET's angle to the magnetic field changed over a wide though variable range. Measured average fluxes are expected to be lower during these times due to trapped particle anisotropy.
2. As noted above, the ~3 month orbital precession caused radiation belt measurements to occur at varying altitude. This is expected to cause a ~3 month periodicity in measured fluxes, which is particularly evident during the spinning intervals.

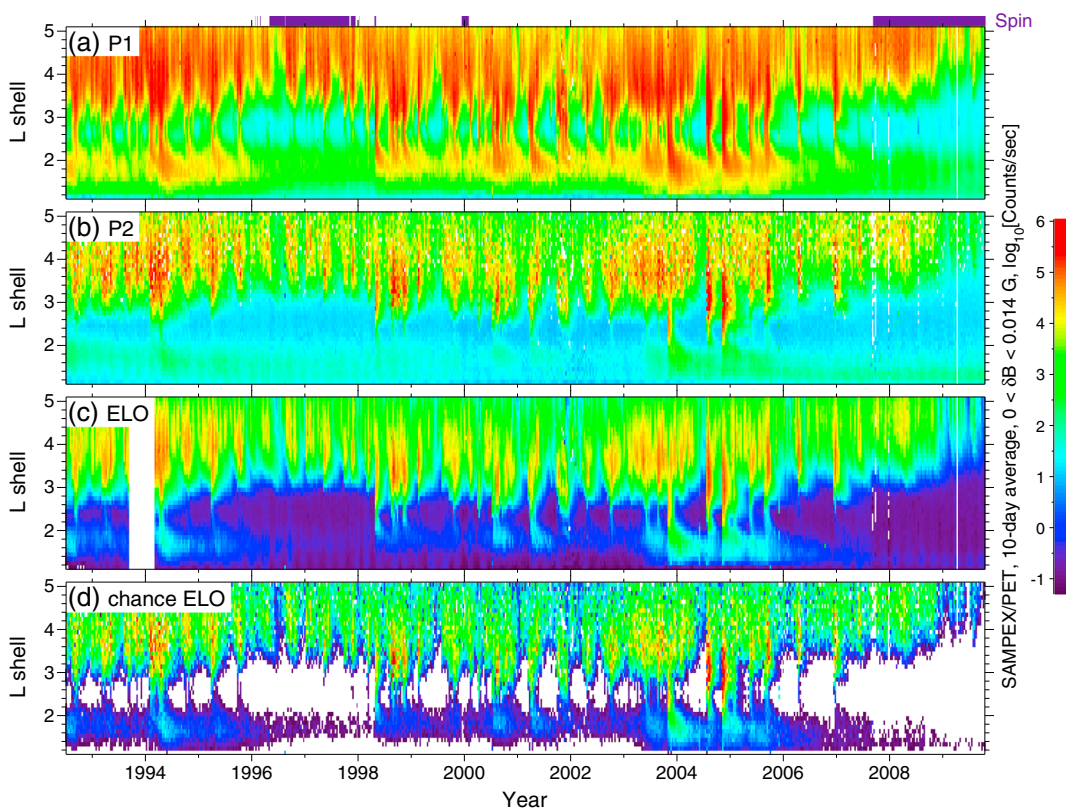


**Figure 4.** Similar to Figure 3 but including only data from the less-stable trapping region,  $0 < \delta B < 0.014$  G.

3. In addition to their electron response, each rate type is also sensitive to protons. For P1 and P2, protons and electrons were included without discrimination; for ELO, protons were actively excluded, as described below, but this was not entirely successful.
4. Measured live times are uncertain and, when they are a small fraction of the 6 s accumulation time, lead to significant uncertainty in the resulting rates. This occurs when rates are high. Changes in live time fraction caused by real changes in low-energy particle flux can, if in error, cause artificial changes in apparent fluxes of higher-energy particles. This is not an important consideration for the current work (but is significant in, for example, the EHI data type).
5. The ELO rate is sensitive to separate particles triggering P1 and P2 within the required resolving time  $\tau$ . That is, instead of a single particle triggering both P1 and P2, one particle triggers P1 and, within the time  $\tau$ , another particle triggers P2; this is referred to as a “chance coincidence”.

The last factor, chance coincidences, is the most serious one for this work, because it can qualitatively change the nature of the ELO measurement. The rate of ELO chance coincidences is [Knoll, 1989, equations (17)–(21)]

$$r_{\text{chance}} = 2\tau r_1 r_2 \quad (1)$$

where  $r_1$  and  $r_2$  are the P1 and P2 rates, respectively. When electron chance coincidences are dominant the energy threshold of ELO is lowered to that of P2 (Figure 2). When chance coincidences formed by an electron in P1 and a proton in P2 are dominant, the ELO electron response threshold is lowered to that of P1. Also, because the chance coincidence rate is proportional to the product  $r_1 r_2$ , the ELO rate is no longer proportional to particle intensity but to its square. Therefore, when the intensity is high enough, depending on the value of  $\tau$ , the chance coincidence rate dominates over the true ELO rate. The resolving time  $\tau$  is not well known. It varies with the size of the pulses from P1 and P2 and depends on whether the first pulse is smaller or larger, but typically is in the range  $\sim 0.5$  to  $1$   $\mu$ s. Using a value  $\tau = 0.5$   $\mu$ s, with measured P1 and P2 rates, the average rate of ELO chance coincidences predicted by equation (1) is shown in Figure 3d.

When the predicted chance ELO rate is equal to the measured ELO rate, or nearly so, then the measured rate is dominated by chance coincidences. Comparing the measured and chance ELO rates (Figures 3c and 3d),

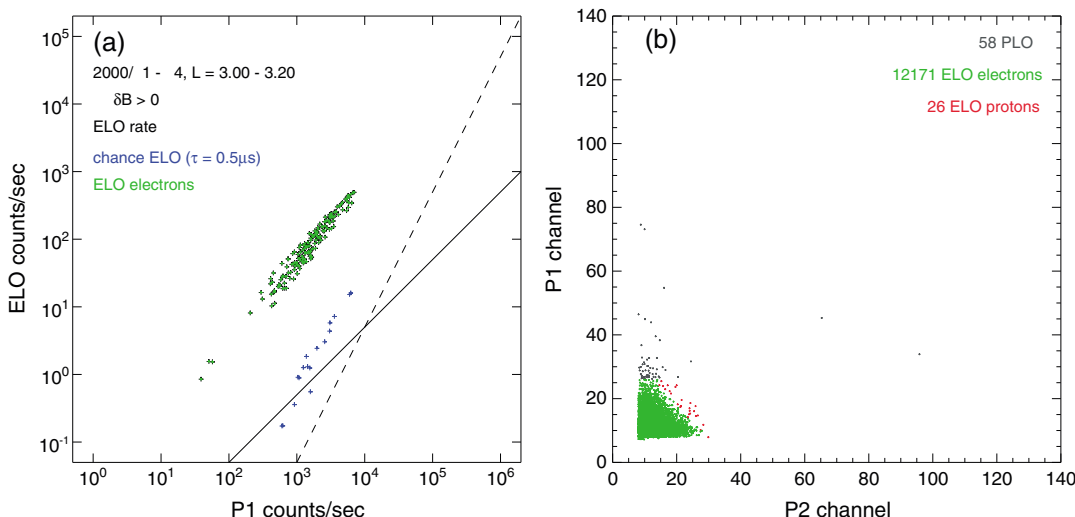


**Figure 5.** Rate and event data from 2000 days-of-year 1 to 4,  $L = 3$  to 3.2. (a) Rate data are shown from ELO versus P1 (black), as are chance ELO rates (blue), and rates of ELO electron events (green). Straight lines have slopes indicating ELO rate proportional to P1 rate (solid) or to the square of the P1 rate (dashed); their magnitudes are arbitrary. (b) Event data show channel numbers, proportional to energy loss, from P1 versus P2, for PLO events (gray), ELO electron events (green), and ELO proton events (red). The number of each event type is listed.

bearing in mind the uncertainty in  $\tau$ , it appears that ELO is dominated by chance coincidences most of the time within the stable trapping region. Only when the measured ELO rate is  $\lesssim 100$  counts/s is this not true. Therefore, Figure 3c should not be considered an accurate representation of the  $E > 1$  MeV electron flux.

The anisotropy of trapped electrons suggests that lower rates should be encountered at higher  $B_m$  values, represented by ranges of smaller  $\delta B$  in Figure 1. This is illustrated in Figure 4, which is similar to Figure 3 except that data are restricted to a less-stable trapping region defined by  $0 < \delta B < 0.014$  G. The highest  $\delta B$  values reached at low  $L$  are  $\sim 0.04$  to 0.05 G (Figure 1), so this is a significant reduction in coverage. As expected, overall flux levels are lower in this region compared to the entire stable trapping region with  $\delta B > 0$ . However, again comparing the measured and chance ELO rates (Figure 4c and 4d), it is apparent that chance coincidences may still be dominant in many instances. (The chance ELO rate is noisy because of sparse P2 data within the more limited trapping region.) Closer examination of the ELO data is necessary to determine its validity as a measure of  $E > 1$  MeV electron flux. This is done in the next section.

## 5. Event Data

In addition to rate data, PET provides event data for certain detector combinations such as ELO. A fraction of all events were included in the telemetered data set. A single event consists of a set of energy loss measurements from each triggered detector, the expectation being that it was formed by a single particle. In the ELO case, that would be an electron passing through P1 and then stopping in P2, or somehow exiting without triggering P3. However, an ELO event can also be formed by a chance coincidence between triggers of P1 and P2.

Event and rate data can be combined to determine particle energy spectra [e.g., Mewaldt *et al.*, 2005; Comess *et al.*, 2013] or to provide insight into the chance coincidence issue as illustrated in Figure 5. In Figure 5a, rates from ELO are shown versus those from P1 during a 4 day interval during 2000 in the  $L$  range 3 to 3.2. Also shown are chance ELO rates computed from the measured P1 and P2 rates. The chance ELO rates are well below measured ELO rates, showing that ELO was operating nominally during this time and the ELO response curve in Figure 2 applies.

Event data from the same time interval are shown in Figure 5b. Channel numbers, proportional to energy loss, from P1 are shown versus those from P2 for each ELO and PLO event. The ELO events have P1 channel  $\leq 26$  and PLO events have P1 channel  $> 26$  (the division is somewhat arbitrary and a few electron events are evident in PLO). The ELO events are further subdivided for this work into those more likely to be formed by electrons or protons, based on calibration data. (Protons can trigger ELO if they pass through the edge of P1, thus leaving a small energy deposit. A few electron events also appear in the ELO proton event region.) The rate of ELO

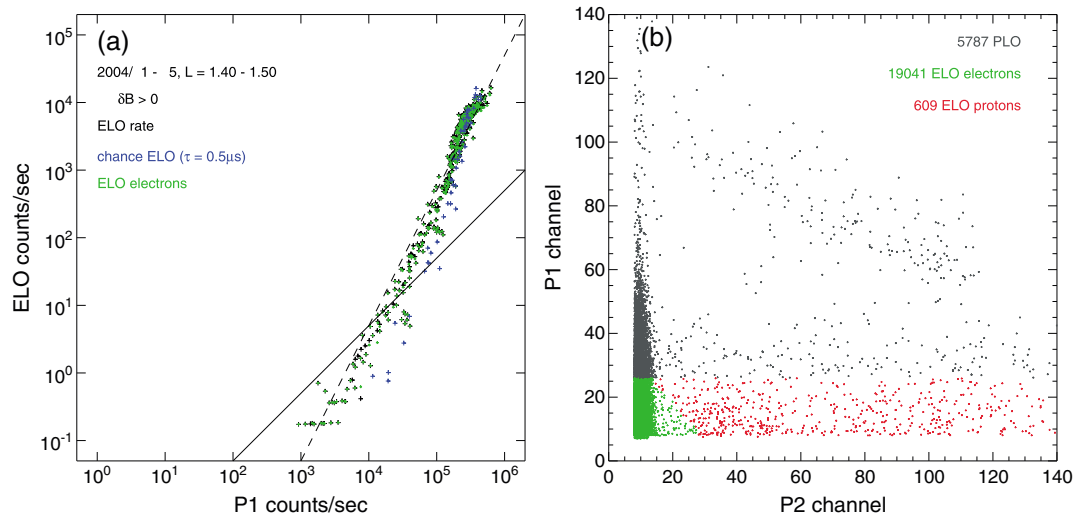


**Figure 6.** Similar to Figure 5 but data are from 2004 days-of-year 1 to 5 and  $L = 1.4$  to 1.5.

electron events are also shown in Figure 5a. They are indistinguishable from the ELO rate data because, in this case, nearly all of the ELO events were from electrons and, with a relatively low event rate, nearly all events were telemetered.

Similar data from a 5 day interval during 2004 and from the  $L$  range 1.4 to 1.5 are shown in Figure 6. The rate data in Figure 6a show that the chance ELO rates are nearly equal to measured ELO rates. In addition, the ELO rates increase approximately in proportion to the square of the P1 rates. Event data in Figure 6b show that ELO events are not confined to the region expected for nominal electron response but extend into the ELO proton event region. Also, the ELO electron event region extends into the PLO event region. These observations together show that the ELO data during this time were dominated by chance coincidences that may have been formed by combinations of electrons or protons separately triggering the P1 and P2 detectors. (Also, ELO is contaminated by protons and PLO by electrons.) The nominal ELO response curve in Figure 2 does not apply to any of the data in this case. This is a result of high proton flux and a high flux of low-energy electrons in the inner radiation belt. (The lower chance ELO rates are below measured ELO rates, but this may be a consequence of the uncertainty in  $\tau$ . A higher  $\tau$  value may be warranted in this case, because chance coincidences result mainly from electrons, rather than from electrons and protons as in other intervals.)

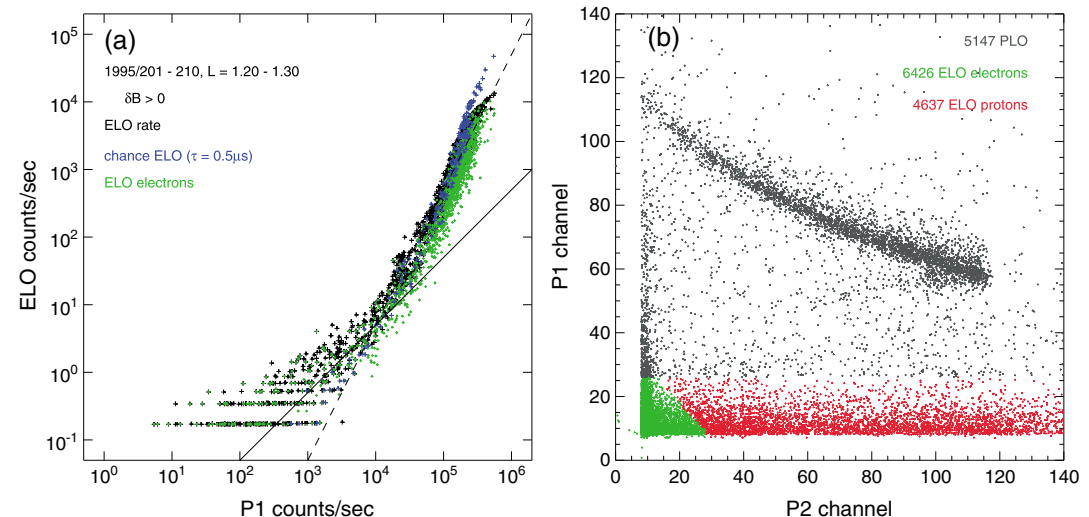


**Figure 7.** Similar to Figure 5 but data are from 1995 days-of-year 201 to 210 and  $L = 1.2$  to 1.3.

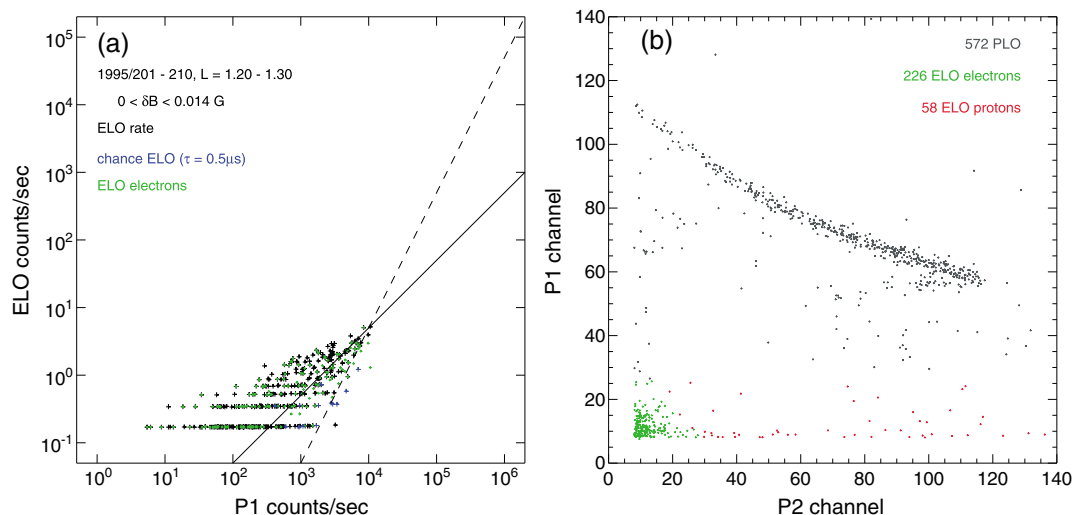


**Figure 8.** Similar to Figure 5 but data are from 1995 days-of-year 201 to 210,  $L = 1.2$  to  $1.3$ , and are restricted to the less-stable trapping region.

Another example of similar data is shown in Figure 7, from a 10 day interval in 1995 and from the  $L$  range 1.2 to 1.3. At these low  $L$  values the trapped proton flux is high, as shown by the clear diagonal track of PLO proton events in Figure 7b. As a result there is considerable proton contamination of the ELO rate, as shown by events in the ELO proton region. Rate data in Figure 7a show that, for a P1 rate  $\gtrsim 10^4$  counts/s, the data are again dominated by chance coincidences because the ELO rate is proportional to the square of the P1 rate and nearly equal to the computed chance ELO rate. However, for lower P1 rates this is not true.

In Figure 8, data are from the same  $L$  range and time interval but restricted to the less-stable trapping region,  $0 < \delta B < 0.014$  G. In this subset the particle fluxes are lower and ELO data are not dominated by chance coincidences ( $\sim 5\%$  of the ELO events are retained and average ELO rate is  $\sim 0.04\%$  of that in Figure 7). Some proton contamination is still present in the ELO rate data but is minimized by considering only the ELO event region where electrons are expected (green in the figure). By restricting event data in this way it is possible, in some cases, to find valid inner belt trapped electron measurements with  $E > 1$  MeV to which the nominal ELO electron response applies.

## 6. Energy Spectra

Where restricted data show only valid ELO electron events, as in Figure 8, it is possible to calculate trapped electron energy spectra. This is done using the subdivided ELO response functions (labeled 1, 2, and 3 in Figure 2). In regions where the P1 rate responds primarily to trapped electrons, which is usually the case, it is also possible to include it, with the P1 response function, to extend the spectra to lower energies. (The P2 rate is not included because it usually responds mainly to protons in the inner belt.) Then there are four data points from which to construct an energy spectrum: the P1 rate, and the rates of ELO event channels 1, 2, and 3 (corrected for the fraction of ELO events telemetered).

For data point  $i$ , the rate  $r_i$  is related to the electron intensity  $j(E)$  and the response function  $G_i(E)$  by

$$r_i = \int G_i(E)j(E)dE \quad (2)$$

To solve for  $j(E)$ , it is assumed to consist of piecewise continuous segments of exponential energy spectra connecting the  $j$  values at four energies: 0.4, 1.1, 1.6, and 2.2 MeV. These correspond approximately to the threshold energies of the four data points. The values of  $j$  at the four energies are determined by solving equation (2), after integrating over the model  $j(E)$ , using Newton's method. As there are four equations for four unknowns the solution is unique (at least locally).

Sample spectra are shown in Figure 9. With a log-linear scale, straight line segments in the figure correspond to the exponential model used in solving equation (2). Spectra are included only for the  $L$  range 1.2 to 1.3 and from time periods in 1994–1995 (Figure 9a) and 2005–2006 (Figure 9b). These intervals were chosen

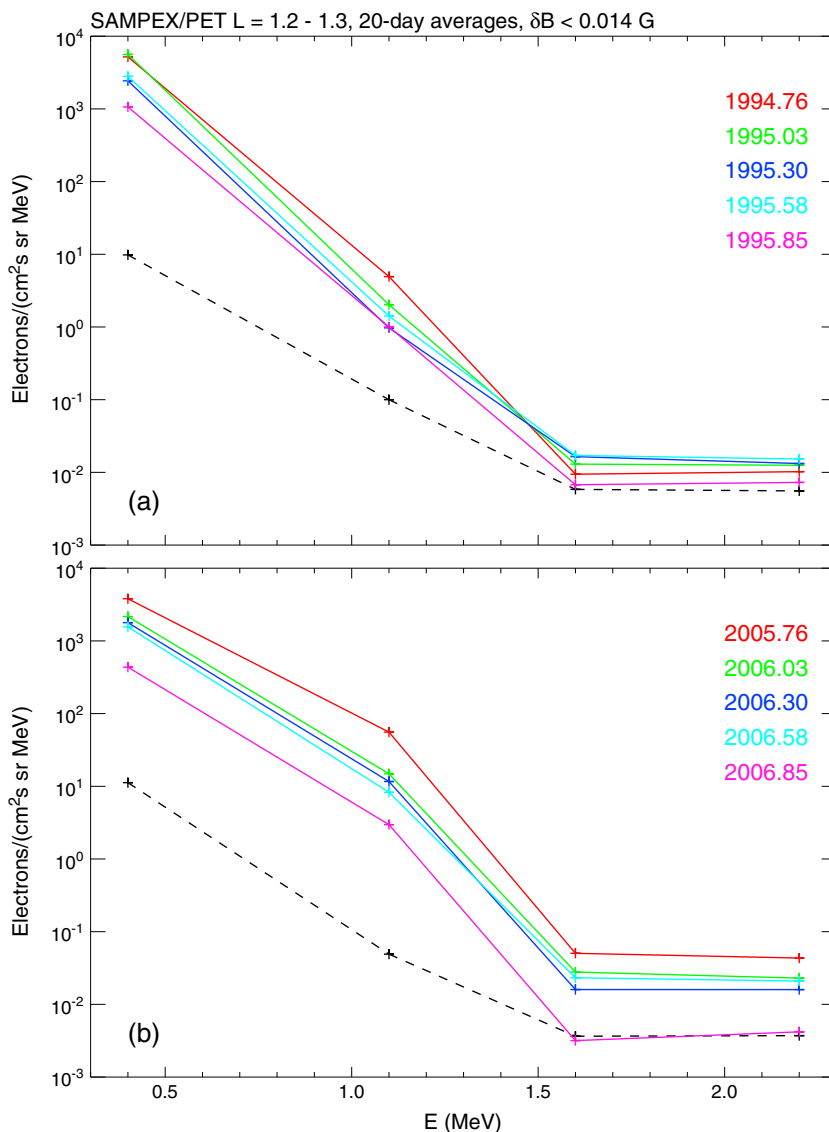


**Figure 9.** Computed electron energy spectra from 20 day averages of P1 and ELO data in the less-stable trapping region (color coded by time in decimal year at the midpoint of each data interval) and from background data in the nontrapping region (dashed).

because trapped electrons were evident above background levels, but their intensity was low enough that chance coincidences were not an issue in the restricted data sets. The trapped electron spectra were computed from data restricted to the region  $0 < \delta B < 0.014$  G. Background spectra computed in the same way with data from the nonstable trapping region ( $\delta B < 0$ ) are also shown. The background can be due to quasi-trapped electrons for the low-energy P1 data [Selesnick, 2012; Li *et al.*, 2015], but for higher energy ELO data ( $E > 1$  MeV), more likely causes are cosmic rays and splash-albedo electrons [Verma, 1967]. Although they are not well resolved by only four data points, comparing to background levels, it appears that the trapped electron spectra are valid up to 1.6 MeV and are background dominated at higher energy. Statistical errors are generally small for these results due to long (20 day) time averages.

## 7. Conclusions

The lower energy electron measurements from SAMPEX/PET, with  $E > 0.35$  MeV (from the P1 detector, Figure 3a), confirm that the inner belt electron intensity below 1 MeV is characterized by occasional rapid increases followed by intervals of slow decay [Rosen and Sanders, 1971]. The increases, or injections, occur across the whole radiation belt, including inner belt, outer belt, and slot region but may be delayed by several

days at lower  $L$ . Contamination by inner belt protons is only a minor factor for this first detector but is a major factor for the second detector (P2, Figure 3b), which showed a significant inner belt electron response only following the 2003 Halloween storm injection. It does confirm that those injected electrons reached energies above 0.63 MeV.

The higher-energy ELO electron data (Figure 3c) were, in the stable trapping region, usually dominated by P1-P2 chance coincidences, as shown by comparison to the computed chance ELO rate (Figure 3d). For the inner belt, where P2 was usually proton dominated, this means that ELO data usually resembled the P1 data, responding to the same  $E > 0.35$  MeV electrons, although after the Halloween storm injection they resembled the P2 data responding to  $E > 0.63$  MeV electrons. (For the outer belt there are no high-energy protons and the  $E > 0.63$  MeV threshold usually applies.)

When electron and proton intensity were low enough the nominal ELO response applies, with  $E > 1.04$  MeV threshold. By restricting data to a less-stable trapping region (Figure 4), chance coincidences are minimized and the nominal response to inner belt electrons is possible. However, to establish whether it applies to a given data interval, it is necessary to examine the ELO event data (Figures 5 to 8). For example, in the several months following the 2003 Halloween storm injection it did not apply and the PET data provide no evidence of  $E > 1$  MeV inner belt or slot region electrons during that interval, although neither do they rule them out. (There is evidence for  $E > 1$  MeV electrons in the slot region from another satellite [Li *et al.*, 2009].)

Sample inner belt electron energy spectra have been computed from restricted PET data to which the nominal ELO response does apply (Figures 8 and 9). They show that trapped inner belt electrons above 1 MeV and up to  $\sim 1.6$  MeV were present during times when the analysis could be performed, which were extended intervals in 1994–1995 and 2005–2006 (others are possible). The soft, approximately exponential spectra, with e-folding energy  $\sim 0.1$  MeV, are typical of those observed at lower energy [Fennell *et al.*, 2015], verifying that simple extrapolation of those low-energy spectra may be appropriate [Li *et al.*, 2015]. There is no clear evidence for the hard electron energy spectra expected from albedo neutron decay [Selesnick, 2015], though they could approach the intensity levels observed above 1.6 MeV interpreted here as untrapped particle background. Slight hardening of the spectra was observed following the active injection period of 2003–2005 (Figure 9b). Intensities were relatively low because of restriction to the low-altitude, less-stable trapping region. Measurement of inner belt electrons above 1 MeV in the more-stable, equatorial trapping region, especially following intense electron injections, will have to await instrumentation capable of operating in that harsh radiation environment.

## Acknowledgments

All data used in this study are available from the SAMPEX data center, <http://www.srl.caltech.edu/sampex/DataCenter>. The author thanks J.M. Albert, W.R. Johnston, X. Li, M.D. Looper, J.P. McCollough, and R.A. Mewaldt for help with the data or comments on the manuscript. This work was supported in part by NASA agreement NNN14AX18I with the Air Force Research Laboratory under the Heliophysics Guest Investigators Program.

Mike Liemohn thanks Natalia Ganushkina, J. Bernard Blake, and another reviewer for their assistance in evaluating this paper.

## References

- Baker, D. N., G. M. Mason, O. Figueroa, G. Colon, J. G. Watzin, and R. M. Aleman (1993), An overview of the Solar Anomalous, and Magnetospheric Particle Explorer (SAMPEX) mission, *IEEE Trans. Geosci. Remote Sens.*, **31**, 531–541, doi:10.1109/36.225519.
- Baker, D. N., S. G. Kanekal, X. Li, S. P. Monk, J. Goldstein, and J. L. Burch (2004), An extreme distortion of the Van Allen belt arising from the ‘Halloween’ solar storm in 2003, *Nature*, **432**, 878–881, doi:10.1038/nature03116.
- Baker, D. N., S. G. Kanekal, R. B. Horne, N. P. Meredith, and S. A. Glauert (2007), Low-altitude measurements of 2–6 MeV electron trapping lifetimes at  $1.5 \leq L \leq 2.5$ , *Geophys. Res. Lett.*, **34**, L20110, doi:10.1029/2007GL031007.
- Comess, M. D., D. M. Smith, R. S. Selesnick, R. M. Millan, and J. G. Sample (2013), Duskside relativistic electron precipitation as measured by SAMPEX: A statistical survey, *J. Geophys. Res. Space Physics*, **118**, 5050–5058, doi:10.1002/jgra.50481.
- Cook, W. R., et al. (1993), PET: A Proton/Electron Telescope for studies of magnetospheric, solar, and galactic particles, *IEEE Trans. Geosci. Remote Sens.*, **31**, 565–571, doi:10.1109/36.225523.
- Fennell, J. F., S. G. Claudepiere, J. B. Blake, T. P. O’Brien, J. H. Clemons, D. N. Baker, H. E. Spence, and G. D. Reeves (2015), Van Allen Probes show the inner radiation zone contains no MeV electrons: ECT/MagEIS data, *Geophys. Res. Lett.*, **42**, 1283–1289, doi:10.1002/2014GL062874.
- Finlay, C. C., et al. (2010), International Geomagnetic Reference Field: the eleventh generation, *Geophys. J. Int.*, **183**, 1216–1230, doi:10.1111/j.1365-246X.2010.04804.x.
- Ginet, G. P., et al. (2013), AE9, AP9 and SPM: New models for specifying the trapped energetic particle and space plasma environment, *Space Sci. Rev.*, **179**, 579–615, doi:10.1007/s11214-013-9964-y.
- Horne, R. B., et al. (2005), Wave acceleration of electrons in the Van Allen radiation belts, *Nature*, **437**, 227–230, doi:10.1038/nature03939.
- Knoll, G. F. (1989), *Radiation Detection and Measurement*, 2nd ed., 754 pp., John Wiley, New York.
- Li, X., A. B. Barker, D. N. Baker, W. C. Tu, T. E. Sarris, R. S. Selesnick, R. Friedel, and C. Shen (2009), Modeling the deep penetration of outer belt electrons during the “Halloween” magnetic storm in 2003, *Space Weather*, **7**, S02004, doi:10.1029/2008SW000418.
- Li, X., R. S. Selesnick, D. N. Baker, A. N. Jaynes, S. G. Kanekal, Q. Schiller, L. Blum, J. Fennell, and J. B. Blake (2015), Upper limit on the inner radiation belt MeV electron intensity, *J. Geophys. Res. Space Physics*, **120**, 1215–1228, doi:10.1002/2014JA020777.
- Looper, M. D., J. B. Blake, R. A. Mewaldt, J. R. Cummings, and D. N. Baker (1994), Observations of the remnants of the ultrarelativistic electrons injected by the strong SSC of 24 March 1991, *Geophys. Res. Lett.*, **21**, 2079–2082.
- Looper, M. D., J. B. Blake, and R. A. Mewaldt (2005), Response of the inner radiation belt to the violent Sun-Earth connection events of October–November 2003, *Geophys. Res. Lett.*, **32**, L03S06, doi:10.1029/2004GL021502.
- Loto’aniu, T. M., I. R. Mann, L. G. Ozeke, A. A. Chan, Z. C. Dent, and D. K. Milling (2006), Radial diffusion of relativistic electrons into the radiation belt slot region during the 2003 Halloween geomagnetic storms, *J. Geophys. Res.*, **111**, A04218, doi:10.1029/2005JA011355.

- Mewaldt, R. A., C. M. S. Cohen, A. W. Labrador, R. A. Leske, G. M. Mason, M. I. Desai, M. D.Looper, J. E. Mazur, R. S. Selesnick, and D. K. Haggerty (2005), Proton, helium, and electron spectra during the large solar particle events of October–November 2003, *J. Geophys. Res.*, **110**, A09S18, doi:10.1029/2005JA011038.
- Roederer, J. G. (1970), *Dynamics of Geomagnetically Trapped Radiation*, 166 pp., Springer, New York.
- Rosen, A., and N. L. Sanders (1971), Loss and replenishment of electrons in the inner radiation zone during 1965–1967, *J. Geophys. Res.*, **76**(1), 110–121, doi:10.1029/JA076i001p00110.
- Selesnick, R. S. (2012), Atmospheric scattering and decay of inner radiation belt electrons, *J. Geophys. Res.*, **117**, A08218, doi:10.1029/2012JA017793.
- Selesnick, R. S. (2015), High-energy radiation belt electrons from CRAND, *J. Geophys. Res. Space Physics*, **120**, 2912–2917, doi:10.1002/2014JA020963.
- Selesnick, R. S., J. B. Blake, and R. A. Mewaldt (2003), Atmospheric losses of radiation belt electrons, *J. Geophys. Res.*, **108**(A12), 1468, doi:10.1029/2003JA010160.
- Shprits, Y. Y., R. M. Thorne, R. B. Horne, S. A. Glauert, M. Cartwright, C. T. Russell, D. N. Baker, and S. G. Kanekal (2006), Acceleration mechanism responsible for the formation of the new radiation belt during the 2003 Halloween solar storm, *Geophys. Res. Lett.*, **33**, L05104, doi:10.1029/2005GL024256.
- Verma, S. D. (1967), Measurement of the charged splash and re-entrant albedo of the cosmic radiation, *J. Geophys. Res.*, **72**(3), 915–925, doi:10.1029/JZ072i003p00915.
- Vette, J. I. (1991), *The AE-8 Trapped Electron Model Environment*, NSSDC/WDC-A-R&S 91-24, NASA Goddard Space Flight Center, Greenbelt, Md.
- Zheng, Y., A. T. Y. Lui, X. Li, and M.-C. Fok (2006), Characteristics of 2–6 MeV electrons in the slot region and inner radiation belt, *J. Geophys. Res.*, **111**, A10204, doi:10.1029/2006JA011748.